

Chaotic motion of the charged test particle in Kerr-MOG black hole with explicit symplectic algorithms

Zhen-Meng Xu¹, Da-Zhu Ma^{2,*}, Wen-Fu Cao³, and Kai-Li¹

¹ *School of Mathematics and Statistics,*

Hubei Minzu University, Enshi 445000, China

² *College of Intelligent Systems Science and Engineering,*

Hubei Minzu University, Enshi 445000, China and

³ *School of Physics and Technology, University of Jinan, Jinan, 250022, China*

Abstract

Recently, Kerr-MOG black hole has attracted widespread research interest and has been widely used in fields such as galaxy rotation curves, gravitational lensing in galaxy clusters, and the formation of large-scale structures in the universe. In this paper, we mainly focus on dynamics of the charged particle around Kerr-MOG black hole. At first, the field equations for the charged particle under the Scalar-Tensor-Vector Gravity (STVG) theory are presented. Then, according to the characteristics of the Hamiltonian system, the Hamiltonian can be decomposed into five integrable parts, and three kinds of explicit symplectic algorithms are constructed. Numerical experiments show that the algorithm (PRK_{64}) is the optimal one. At last, the Poincaré section and the fast Lyapunov indicator (FLI) are used to explore dynamic evolution of the particle. From the numerical results, it is easy to find that the energy E , the angular momentum L , the magnetic field parameter β , the black hole spin parameter a , and the gravitational field strength parameter α have an impact on the motion of the particle. In particular, the chaotic region increases as E , β , or α increases, but decreases with the increases of a or L . Moreover, when any two of the five parameters are applied simultaneously, it is easy to observe that a and L play a dominant role.

* mdzhbmy@126.com, Corresponding author

I. INTRODUCTION

As is well known, Einstein's general theory of relativity, one of the foundations of modern physics, has successfully explained many astronomical and gravitational phenomena. However, it has limitations in explaining the properties of dark matter and dark energy, unifying quantum mechanics and gravity, resolving the singularity of black holes, and explaining the origin of the accelerating expansion of the universe and the formation of large-scale structures [1]. Based on these limitations, modified theories such as the modified Newtonian Dynamics (MOND) theory, the STVG theory, and other modified theories that attempt to extend the general theory of relativity by adding new field variables or modified equations, have been successively proposed to extend the applications of general relativity. For example, Camilloni et al. [2] explored magnetospheric models and black hole jet emissions in the Modified Gravity (MOG) context. Moreover, Jai-akson et al. [3] discussed the main possible features of black hole mergers in the Einstein-Maxwell-dilaton theory.

It is shown that more than 70% of the universe is composed of dark energy, which is the primary driver of the accelerated expansion of the universe [1, 4]. Additionally, the existence of dark matter can be inferred from some phenomena such as galaxy rotation curves, gravitational lensing, and the cosmic microwave background radiation. Dark matter is estimated to constitute at least 20% of the universe's matter content. Since no direct detection evidence for dark matter has emerged, some theories attempt to explain existing astronomical observations without introducing dark matter. Milgrom [5] first proposed a theory to explain astrophysical phenomena without dark matter, known as the MOND theory. By modifying the laws of gravity, MOND successfully explains galaxy rotation curves and the motion of low-surface-brightness galaxies, but its applicability on galaxy cluster and cosmological scales is limited, making it unable to fully replace dark matter models.

Subsequently, Moffat [6] proposed another theory without assuming the existence of dark matter, namely the STVG theory, also known as the MOG theory, as an alternative method to dark matter models. The STVG theory has been widely used to explain gravitational phenomena that cannot be fully explained by standard general relativity and dark matter models. In the assumption that dark matter does not exist in the universe, the STVG theory not only describes the dynamics of galaxies [7–10], but also explains the solar system, the growth of structures, and the cosmic microwave background (CMB) sound power spectrum

data [11, 12]. In the STVG theory, the addition of a vector field and a variable gravitational constant affects the gravitational action, making objects such as orbiting particles near black holes experience non-standard gravitational effects. Moffat [13] inferred that the gravitational field strength parameter α increases the shadow radius by studying the MOG black hole. Lee and Han [14] found that α contributes to the inner stable circular orbit (ISCO) radius by studying Kerr-MOG black hole. Guo et al. [15] studied the shadows cast by near-extremal Kerr-MOG black holes for different values of the parameter in MOG. Hou et al. [16] investigated the observational phenomena of Kerr-Melvin black holes under the illumination of accretion disks.

Besides, dynamics of the charged and neutral particles near black holes is an important research topic in the field of relativistic astrophysics. For example, Battista and Esposito [17] carried out a systematic study on the geodesic motion in Euclidean Schwarzschild geometry. Dutta et al. [18] studied the dynamics of circular geodesics (chargeless massive particle) and pulsating classical string in the p-brane background. Dalui et al. [19, 20] found that the existence of the event horizon makes the motion of particles chaotic. It has been reported that the numerical method plays a key role in chaotic dynamics, because the numerical errors may result in pseudo chaos [21]. For the Hamiltonian systems, the symplectic method is the optimal algorithm [22]. The symplectic algorithm proposed by Feng [23] is a high-order implicit symplectic method based on the implicit midpoint approach, suitable for non-separable Hamiltonian systems. Ruth [24] further proposed an explicit symplectic algorithm, dividing the Hamiltonian system into kinetic energy T and potential energy V , thereby preserving the symplectic structure. Research has shown that explicit symplectic algorithms are generally not directly applicable to inseparable Hamiltonian systems, making implicit symplectic algorithms more suitable. Implicit symplectic algorithms include semi-implicit symplectic algorithms and implicit midpoint methods [25–32]. Although implicit symplectic algorithms can be applied to any Hamiltonian system, they are less computationally efficient compared to explicit symplectic methods [32, 33]. Thus, the development of explicit symplectic algorithms is particularly important. Then, the force-gradient symplectic algorithm was proposed, which effectively avoids the appearance of negative time coefficients by introducing a force gradient operator [34]. Ruth [24] and Chin [35, 36] constructed the third and fourth order force gradient symplectic algorithms respectively. A symplectic integrator with third-order potential derivatives was developed by Sun et al. [37]. Recently,

Wu et al. [38] have constructed an explicit symplectic integrator with adaptive time steps in curved spacetime, which provides a great help to study Hamiltonian with anticipated separations.

In terms of the construction of symplectic integrators in black hole spacetime, Wang et al. [39–41] constructed explicit symplectic integrators for Schwarzschild, Reissner-Nordström, and Reissner–Nordström-(anti)-de sitter black holes by dividing Hamiltonian systems into multiple integrable sub-Hamiltonian systems. In addition, Wu et al. [42] constructed an explicit symplectic integrator for Kerr black hole spacetime by using time transformation methods [43]. Since then, construction of the explicit symplectic integrators in curved spacetimes aroused much attention. Hu and Huang [44] utilized explicit symplectic integrators to study chaos in a magnetized Brane-World spacetime. Zhou et al. [45] discussed the chaotic motion of charged test particles in a magnetized Schwarzschild black hole. Cao et al. [46] studied the electromagnetic fields and chaotic motion of charged particles around hairy black holes in Horndeski gravity. Lu and Wu [47] analyzed the effects of two quantum correction parameters on the chaotic dynamics of particles near modified Schwarzschild black hole under the renormalization group. These studies show that the combination of gravity theory and symplectic algorithm provides an effective tool for relativistic astrophysics, helping to further reveal the deep mechanism of dark matter, dark energy and black hole gravitational phenomena.

Therefore, in order to explore chaotic dynamics in Kerr-MOG black hole, it is necessary to fully consider the accuracy and stability of numerical methods. Fortunately, with the help of the time transformation method, the Hamiltonian in Kerr-MOG black hole can be converted into a new form. Due to the fact that the new Hamiltonian can be decomposed into several integrable parts, the explicit symplectic algorithms can be applied. With high-precision numerical solutions, the chaotic phenomenon of particles can be accurately described [48]. This paper is organized as follows, the field equations under the STVG theory are briefly introduced in Section II, three explicit symplectic algorithms are constructed in Section III, effects of varying parameters on the motion of the charged particle near Kerr-MOG black hole are discussed in Section IV, the final conclusions are given in Section V.

II. THE BLACK HOLE MODEL

In this section, we first provide the field equations and gravitational effects in STVG, then derive the black hole solution of Kerr-MOG based on the MOG theory. At last, by using the electromagnetic four-potential, we obtain the external asymptotically uniform magnetic field around the black hole.

A. STVG field equations

STVG theory [49] is a covariant theory of gravity, in which, the gravitational field action is mainly composed of Einstein's gravitational action S_G , vector field S_ϕ , scalar field S_S , and matter field S_M ,

$$S = S_G + S_\phi + S_S + S_M. \quad (1)$$

Here,

$$S_G = \frac{1}{16\pi} \int \frac{1}{G} (R + 2\Lambda) \sqrt{-g} d^4x, \quad (2)$$

where $R = g^{\mu\nu} R_{\mu\nu}$ and Λ represent the Ricci tensor and the cosmological constant, respectively. Considering an anti-symmetric field $B_{\mu\nu}$ is formed out of the vector field ϕ_μ , and $B_{\mu\nu} = \partial_\mu \phi_\nu - \partial_\nu \phi_\mu$, we have

$$S_\phi = -\frac{1}{4\pi} \int [\mathcal{K} + V(\phi_\mu)] \sqrt{-g} d^4x, \quad (3)$$

where $\mathcal{K} = \frac{1}{4} B^{\mu\nu} B_{\mu\nu}$ is the kinetic term for the ϕ_μ field.

$$S_S = \int \frac{1}{G} \left[\frac{1}{2} g^{\alpha\beta} \left(\frac{\nabla_\alpha G \nabla_\beta G}{G^2} + \frac{\nabla_\alpha \mu \nabla_\beta \mu}{\mu^2} \right) - \frac{V_G(G)}{G^2} - \frac{V_\mu(\mu)}{\mu^2} \right] \sqrt{-g} d^4x, \quad (4)$$

∇_α denotes the covariant derivation with respect to the metric $g_{\alpha\beta}$. $V(\phi_\mu)$, $V_G(G)$ and $V_\mu(\mu)$ are the self-interaction potentials associated with the vector field and the scalar fields.

$$S_M = - \int (\rho \sqrt{u^\mu u_\mu} + Q u^\mu \phi_\mu) \sqrt{-g} d^4x + J^\mu \phi_\mu, \quad (5)$$

$u^\mu = dx^\mu/d\tau$ represents a timelike velocity, τ denotes the proper time along a timelike geodesic.

The covariant current density is written as $J^\mu = \kappa \rho_M u^\mu$, ρ_M and ρ are the density of matter, $\kappa = \sqrt{\alpha G_N}$. Here, $\alpha = (G - G_N)/G_N$ denotes the scalar field, G_N is Newton's gravitational constant, $Q = \sqrt{\alpha G_N} M$ is the gravitational source charge, which is related to the mass density.

The modified gravitational field equations are presented as follows,

$$G_{\mu\nu} = -\frac{8\pi G}{c^4} T_{\phi\mu\nu}. \quad (6)$$

Here, $c = 1$, the gravitational coupling $G = G_N(1 + \alpha)$ is constant with $\partial_\nu G = 0$. The energy-momentum tensor for the ϕ_μ vector field is defined as

$$T_{\phi\mu\nu} = -\frac{1}{4\pi} (B_\mu^\alpha B_{\nu\alpha} - \frac{1}{4} g_{\mu\nu} B^{\alpha\beta} B_{\alpha\beta}), \quad (7)$$

with

$$\Delta_\nu B^{\mu\nu} = 0, \Delta_\sigma B_{\mu\nu} + \Delta_\mu B_{\nu\sigma} + \Delta_\nu B_{\mu\sigma} = 0. \quad (8)$$

For simplicity, we set the potentials of the fields to zero, $V(\phi_\mu) = V(G) = V(\mu) = 0$. Thus, S_ϕ contains only the kinetic term, which can be considered as a function of the massive vector field invariant $\mathcal{B} = B_{\mu\nu} B^{\mu\nu}$, and the kinetic term is expressed as $\mathcal{K} = f(\mathcal{B})$.

B. The Kerr-MOG black hole solution

This section gives a kinetic model for the motion of the charged particle around Kerr-MOG black hole in an external uniform magnetic field, where the MOG equations are axisymmetric, smooth, and asymptotically flat. The Kerr metric in modified gravity [50], derived from our gravitational field equations, takes the following form in Boyer-Lindquist coordinates (t, r, θ, ϕ) of

$$ds^2 = g_{tt} dt^2 + g_{rr} dr^2 + g_{\theta\theta} d\theta^2 + g_{\phi\phi} d\phi^2 + 2g_{t\phi} dt d\phi. \quad (9)$$

Where,

$$g_{tt} = -\left(\frac{\Delta - a^2 \sin^2 \theta}{\Sigma}\right), g_{rr} = \frac{\Sigma}{\Delta}, g_{\theta\theta} = \Sigma, \quad (10)$$

$$g_{\phi\phi} = \frac{\sin^2 \theta}{\Sigma} [(a^2 + r^2)^2 - a^2 \sin^2 \theta \Delta],$$

$$g_{t\phi} = \frac{a \sin^2 \theta}{\Sigma} [\Delta - (a^2 + r^2)]. \quad (11)$$

In which,

$$\begin{aligned}\Delta &= r^2 - 2GMr + a^2 + \alpha GG_N M^2, \\ \Sigma &= r^2 + a^2 \cos^2 \theta.\end{aligned}\tag{12}$$

The Kerr-MOG solution is fully described by the mass M , the spin parameter a , and the strength of the gravitational field parameter α . It should be noted here that the Arnowitt-Deser-Misner (ADM) mass M_α is connected to M through the relation $M_\alpha = (1 + \alpha)M$. The horizons in the spacetime of Kerr-MOG black hole are identified by the roots of the equation,

$$\Delta = r^2 - 2M_\alpha r + a^2 + \frac{\alpha}{(1 + \alpha)} M_\alpha^2 = 0.\tag{13}$$

As a result,

$$r_\pm = M_\alpha \pm \sqrt{\frac{M_\alpha^2}{(1 + \alpha)} - a^2}.\tag{14}$$

Moreover, the extremal limit for Kerr-MOG black hole can be written as $M_\alpha^2 = (1 + \alpha)a^2$. By using the dimensionless processing $r \rightarrow r/G_N M$, $a \rightarrow a/G_N M$, $\alpha \rightarrow \alpha/G_N M$, Δ can be simplified to

$$\Delta = r^2 - 2(1 + \alpha)r + a^2 + \alpha(1 + \alpha).\tag{15}$$

C. Electromagnetic Four-Potential

In rotating spacetime, the vector potential can be further generalized as follows,

$$\Phi_\mu = \frac{\sqrt{\alpha}Mr}{\Sigma}(-1, 0, 0, a \sin^2 \theta).\tag{16}$$

An external asymptotically uniform magnetic field B surrounding Kerr-MOG black hole is assumed to be perpendicular to the equatorial plane $\theta = \pi/2$. The same as in [51], an electromagnetic four-potential with two nonzero covariant components was proposed by using Wald's method [52],

$$A_t = \frac{B}{2}g_{t\phi} - \frac{Q_W}{2}, A_\phi = \frac{B}{2}g_{\phi\phi}.\tag{17}$$

Here, we set $Q_W = 2aBM$. Based on Eq. (11), Eq. (17) can be simplified to

$$\begin{aligned} A_t &= \frac{aB \sin^2 \theta (\Delta - (a^2 + r^2))}{2\Sigma} - aB, \\ A_\phi &= \frac{B \sin^2 \theta \left((a^2 + r^2)^2 - a^2 \Delta \sin^2 \theta \right)}{2\Sigma}. \end{aligned} \quad (18)$$

III. CONSTRUCTION OF THE EXPLICIT SYMPLECTIC INTEGRATORS

In this section, we first give the equations of motion of the charged particle, and then construct the explicit symplectic algorithms, which are used to solve the Hamiltonian system of Kerr-MOG spacetime.

A. Hamiltonian system

If we consider a particle with charge q orbiting Kerr-MOG black hole in the presence of the external magnetic field (18), and we set $p^\mu p_\mu = -m^2$. Thus, by employing the method of variable separation, the charged particle motion corresponding to the metric (9) can be described by the Hamilton–Jacobi equation [51],

$$\begin{aligned} H &= -\frac{\partial S}{\partial \tau} \\ &= \frac{1}{2} g^{\mu\nu} (p_\mu - qA_\mu + \tilde{q}\Phi_\mu)(p_\nu - qA_\nu + \tilde{q}\Phi_\nu) \\ &\quad + \frac{1}{2} m^2. \end{aligned} \quad (19)$$

Here, $\tilde{q} = \sqrt{\alpha}m$ and m^2 represent gravitational test particle charge and the rest mass, respectively. $p_\mu = \partial S / \partial x^\mu$ is the four-momentum of particles. There are two motion constants, they are the energy and angular momentum of the test particle.

$$-E = p_t = g_{tt}\dot{t} + g_{t\phi}\dot{\phi} + qA_t + \tilde{q}\Phi_t, \quad (20)$$

$$L = p_\phi = g_{t\phi}\dot{t} + g_{\phi\phi}\dot{\phi} + qA_\phi + \tilde{q}\Phi_\phi. \quad (21)$$

Where, the dot is the derivative with respect to the proper time τ . The Hamiltonian in Eq. (19) is modified as follows,

$$H = H_p(r, \theta) + \frac{\Delta}{2\Sigma} p_r^2 + \frac{1}{2\Sigma} p_\theta^2, \quad (22)$$

$$\begin{aligned}
H_p(r, \theta) = & \frac{1}{2}[g^{tt}(E + qA_t - \tilde{q}\Phi_t)^2 \\
& + g^{\phi\phi}(L - qA_\phi + \tilde{q}\Phi_\phi)^2 \\
& - 2g^{t\phi}(E + qA_t - \tilde{q}\Phi_t)(L - qA_\phi + \tilde{q}\Phi_\phi) \\
& + 1].
\end{aligned} \tag{23}$$

$H_p(r, \theta)$ denotes the potential component of the Hamiltonian. Meanwhile, the motion of the charged test particle can be limited by the energy boundaries defined by $H = 0$. Substituting Eqs. (10)-(12) and Eq. (16) into Eqs. (22) and (23), the form of the Hamiltonian in the magnetized Kerr-MOG black hole can be explicitly expressed as

$$\begin{aligned}
H_p(r, \theta) = & \frac{1}{2}(1 + ((a^2 + 2(r^2 - 2r(1 + \alpha)) + \alpha(1 \\
& + \alpha)) + a^2 \cos 2\theta)(a^2 \beta(a^2 + r^2 - 2r(1 + \alpha)) + \alpha(1 \\
& + \alpha)) - (a^4 \beta + 2a^2 \beta r^2 + \beta r^4 - 2ar\alpha - 2a^2 L \cot^2 \theta) \\
& \csc^2 \theta + 2Lr^2 \csc^4 \theta)^2 \sin^6 \theta) / ((a^2 + r^2 - 2r(1 + \alpha) \\
& + \alpha(1 + \alpha))(a^2 + 2r^2 + a^2 \cos 2\theta)^3) + (2(-2r(Er \\
& - a\beta r + \alpha) + 2a^2(-E + a\beta) \cos^2 \theta + a\beta(2r - \alpha) \\
& (1 + \alpha) \sin^2 \theta)^2 (- (a^2 + r^2)^2 + a^2(a^2 + r^2 - 2r(1 \\
& + \alpha) + \alpha(1 + \alpha)) \sin^2 \theta)) / ((a^2 + r^2 - 2r(1 + \alpha) \\
& + \alpha(1 + \alpha))(a^2 + 2r^2 + a^2 \cos 2\theta)^3) + (4a(1 + \alpha) \\
& (-2r + \alpha)(-2r(Er - a\beta r + \alpha) + 2a^2(-E + a\beta) \\
& \cos^2 \theta + a\beta(2r - \alpha)(1 + \alpha) \sin^2 \theta)(2Lr^2 + 2a^2 L \\
& \cos^2 \theta - (a^4 \beta + 2a^2 \beta r^2 + \beta r^4 - 2ar\alpha) \sin^2 \theta + a^2 \\
& \beta(a^2 + r^2 - 2r(1 + \alpha) + \alpha(1 + \alpha)) \sin^4 \theta)) / ((a^2 \\
& + r^2 - 2r(1 + \alpha) + \alpha(1 + \alpha))(a^2 + 2r^2 + a^2 \cos 2\theta)^3).
\end{aligned} \tag{24}$$

Here, $\beta = qB$.

B. Explicit symplectic algorithms

The same as in [39], a splitting technique is used here. For the Hamiltonian (22), it can be splitted to five parts

$$H = H_1 + H_2 + H_3 + H_4 + H_5. \tag{25}$$

Where,

$$\begin{aligned}
H_1 &= H_p(r, \theta), \\
H_2 &= \frac{a^2 + \alpha(1 + \alpha)}{2\Sigma} p_r^2, \\
H_3 &= \frac{r^2 p_r^2}{2\Sigma}, \\
H_4 &= \frac{-r(1 + \alpha)}{\Sigma} p_r^2, \\
H_5 &= \frac{p_\theta^2}{2\Sigma}.
\end{aligned} \tag{26}$$

It is clear that the sub-Hamiltonian function obtained by this decomposition method is not capable of constructing an explicit symplectic integrator [42]. In order to solve this problem, the time transformation function $d\tau = g(r, \theta)dw$ is adopted. Here, τ is the proper time, and w is a newly introduced coordinate time. By means of the time-transformation function $g(r, \theta) = \frac{\Sigma}{r^2}$, a new Hamiltonian is obtained,

$$\mathcal{H} = \frac{\Sigma}{r^2} H_1 + \frac{\Delta}{2r^2} p_r^2 + \frac{1}{2r^2} p_\theta^2. \tag{27}$$

\mathcal{H} is limited by the constraint $\mathcal{H} = 0$. As the Σ function is eliminated in the denominators of the second and third terms in the new Hamiltonian \mathcal{H} , \mathcal{H} is integrable. Thus, \mathcal{H} can also be decomposed into the following five parts,

$$\mathcal{H} = \mathcal{H}_1 + \mathcal{H}_2 + \mathcal{H}_3 + \mathcal{H}_4 + \mathcal{H}_5. \tag{28}$$

Each of the subsidiary Hamiltonian systems is as follows,

$$\begin{aligned}
\mathcal{H}_1 &= \frac{\Sigma}{r^2} H_1, \\
\mathcal{H}_2 &= \frac{a^2 + \alpha(1 + \alpha)}{2r^2} p_r^2, \\
\mathcal{H}_3 &= \frac{p_r^2}{2}, \\
\mathcal{H}_4 &= \frac{-(1 + \alpha)}{r} p_r^2, \\
\mathcal{H}_5 &= \frac{p_\theta^2}{2r^2}.
\end{aligned} \tag{29}$$

The equations of motion for the sub-Hamiltonian \mathcal{H}_1 in terms of the new coordinate time

are expressed as

$$\begin{aligned}
\frac{d\tau}{dw} &= \frac{\Sigma}{r^2} = g(r, \theta), \\
\frac{dp_r}{dw} &= -\frac{\partial \mathcal{H}_1}{\partial r} = P_r(r, \theta), \\
\frac{dp_\theta}{dw} &= -\frac{\partial \mathcal{H}_1}{\partial \theta} = P_\theta(r, \theta).
\end{aligned} \tag{30}$$

The equations of motion for the rest sub-Hamiltonians are given as following,

$$\begin{aligned}
\mathcal{H}_2 : \frac{dr}{dw} &= \frac{(a^2 + \alpha(1 + \alpha))}{r^2} p_r, \\
\frac{dp_r}{dw} &= \frac{(a^2 + \alpha(1 + \alpha))}{r^3} p_r^2. \\
\mathcal{H}_3 : \frac{dr}{dw} &= p_r, \frac{dp_r}{dw} = 0. \\
\mathcal{H}_4 : \frac{dr}{dw} &= \frac{-2(1 + \alpha)}{r} p_r, \\
\frac{dp_r}{dw} &= \frac{-(1 + \alpha)}{r^2} p_r^2. \\
\mathcal{H}_5 : \frac{d\theta}{dw} &= \frac{p_\theta}{r^2}, \frac{dp_r}{dw} = \frac{p_\theta^2}{r^3}.
\end{aligned} \tag{31}$$

The analytic solutions for each of the five splitting parts are explicitly expressed in terms of the new time variable w . Given the initial values of $(r_0, \theta_0, p_{r_0}, p_{\theta_0})$, the analytic solution for each part can be written as

$$\begin{aligned}
\tau(w) &= \tau_0 + wg(r_0, \theta_0). \\
\mathcal{H}_1 : p_r(w) &= p_{r_0} + w \left(-\frac{\partial \mathcal{H}_1}{\partial r} \right), \\
p_\theta(w) &= p_{\theta_0} + w \left(-\frac{\partial \mathcal{H}_1}{\partial \theta} \right). \\
\mathcal{H}_2 : r(w) &= (2(a^2 + \alpha(1 + \alpha))p_{r_0}w/r_0 + r_0^2)^{\frac{1}{2}}, \\
p_r(w) &= \frac{p_{r_0}}{r_0} (2(a^2 + \alpha(1 + \alpha))p_{r_0}w/r_0 + r_0^2)^{\frac{1}{2}}. \\
\mathcal{H}_3 : r(w) &= r_0 + wp_{r_0}. \\
\mathcal{H}_4 : r(w) &= ((-3(1 + \alpha)wp_{r_0} + r_0^2)^2 / r_0)^{\frac{1}{3}}, \\
p_r(w) &= p_{r_0} ((-3(1 + \alpha)wp_{r_0} + r_0^2) / r_0^2)^{\frac{1}{3}}. \\
\mathcal{H}_5 : \theta(w) &= \theta_0 + wp_{\theta_0} / r_0^2, \\
p_r(w) &= p_{r_0} + wp_{\theta_0}^2 / r_0^3.
\end{aligned} \tag{32}$$

If we set the time step h invariant, a second-order explicit symplectic integrator is constructed to solve the Hamiltonian (27). It is presented as

$$S_2^{\mathcal{H}}(h) = \chi_{h/2} \times \chi_{h/2}^*, \quad (33)$$

and the two first-order solvers are

$$\chi_h = \mathcal{H}_5(h) \times \mathcal{H}_4(h) \times \mathcal{H}_3(h) \times \mathcal{H}_2(h) \times \mathcal{H}_1(h), \quad (34)$$

$$\chi_h^* = \mathcal{H}_1(h) \times \mathcal{H}_2(h) \times \mathcal{H}_3(h) \times \mathcal{H}_4(h) \times \mathcal{H}_5(h). \quad (35)$$

Then, a fourth-order explicit symplectic integrator is derived through the symmetric combination of three second-order methods [53].

$$S_4^{\mathcal{H}}(h) = S_2^{\mathcal{H}}(\gamma h) \times S_2^{\mathcal{H}}(\delta h) \times S_2^{\mathcal{H}}(\gamma h), \quad (36)$$

where $\gamma = 1/(1 - \sqrt[3]{2})$ and $\delta = 1 - 2\gamma$. Besides, a fourth-order optimal explicit symplectic *PRK* algorithm(*PRK*₆₄) [54] with first-order operators χ_h and χ_h^* is proposed,

$$PRK_{64} = \chi_{c_{12}h} \times \chi_{c_{11}h}^* \times \cdots \times \chi_{c_{2}h}^* \times \chi_{c_1h}. \quad (37)$$

Here, the time coefficients are

$$c_1 = c_{12} = 0.079203696431196,$$

$$c_2 = c_{11} = 0.130311410182166,$$

$$c_3 = c_{10} = 0.2222861495867608,$$

$$c_4 = c_9 = -0.366713269047426,$$

$$c_5 = c_8 = 0.324648188689706,$$

$$c_6 = c_7 = 0.109688477876750.$$

To evaluate the performance of *S2*, *S4* and *PRK*₆₄, numerical experiments are conducted. We set $h = 1$, $E = 0.995$, $L = 4.6$, $\beta = 4 \times 10^{-4}$, $a = 0.5$ and $\alpha = 0.2$. The initial conditions are $\theta = \pi/2$, $p_r = 0$, p_θ is obtained from Eq. (27), and the integration time is 10^7 . The results are shown in Figs. 1(a)-1(b), the left panel (a) is for $r = 11$, and the right panel (b) is for $r = 110$. It is found that *S2*, *S4* and *PRK*₆₄ have good performance in preserving the Hamiltonian error $\Delta\mathcal{H}$. However, the accuracy of *S4* is two orders of magnitude higher than that of *S2*, but two orders of magnitude lower than that of *PRK*₆₄. Therefore, *PRK*₆₄ is the best in performance, which is adopted in the subsequent calculations.

IV. DYNAMICS OF THE CHARGED PARTICLE

Many chaos indicators have been proposed in literature, such as the Poincaré section method, the Lyapunov exponent, FLI, the 0-1 indicator, and spectral analysis. It has been reported that the Poincaré section method and FLI are simple and easy to implement methods [21, 55], so they are used in this paper. Especially, the Poincaré section method is particularly suitable for studying four-dimensional conservative systems with two degrees of freedom. For example, the phase space structures of the orbits 1 and 2 in Figs. 1(a)-1(b) can be depicted by using the Poincaré sections on the two-dimensional $r - Pr$ plane. These points in panel (r, Pr) are obtained through linear interpolation on the section $\theta = \pi/2$. As shown in Fig. 1(c), the red points form a closed curve, indicating that the orbit 1 is regular. In contrast, the blue points are randomly distributed, which implies that the orbit 2 is chaotic.

FLI is a widely used tool for distinguishing between regular and chaotic orbits, and it overcomes the limitations of the Poincaré section method in three-dimensional dynamical systems. Moreover, it distinguishes regular and chaotic orbits more quickly and sensitively than other indicators [55]. By using the two nearby-orbit method [56, 57], we have $FLI = \log_{10} \frac{d(w)}{d(0)}$, where $d(w)$ and $d(0)$ represent the distances between two nearby orbits at time w and the initial time, respectively. As shown in Fig. 1(d), for the regular orbit 1, FLI increases linearly with time; while for the chaotic orbit 2, FLI increases exponentially with time.

It is easy to conclude from Fig. 1 that the initial position of the particle is very important for the dynamical evolution. For example, under the same conditions, $r = 11$ corresponds to an ordered orbit, while $r = 110$ is associated with the chaotic orbit. Besides, the energy E , the angular momentum L , the magnetic field parameter β , the black hole spin parameter a , and the gravitational field strength parameter α may influence dynamics of the system, too. These situations will be discussed in the next subsection.

A. The impact of a single parameter

In order to detect the impact of changing the parameters on the shift from regular to chaotic regimes, effects of E , L , β , a , and α on dynamics of the particle will be analyzed in

this section.

(1) In case of $r=11$. At first, we set $L = 4.6$, $\beta = 4 \times 10^{-4}$, $a = 0.5$ and $\alpha = 0.2$, and let $E \in [0.990, 0.999]$. $E = 0.991$, $E = 0.994$, $E = 0.998$ and $E = 0.999$ represent four different orbits 1, 2, 3 and 4, respectively. The results from Poincaré section are shown in Fig. 2(a), it is found that the orbit 1 is in order, the orbit 2 is quasi-periodic, the orbits 3 and 4 are chaotic. This tells us that the system has a transition from order to chaos as E increases. Next, if E is invariant but L is variant, the situation is different. For example, $E = 0.995$, $\beta = 8.9 \times 10^{-4}$, $a = 0.5$ and $\alpha = 0.08$, let $L \in [3.8, 4.6]$. The results are given in Fig. 2(b), $L = 3.8$, $L = 4.1$, $L = 4.4$ and $L = 4.6$ denote four trajectories. We find that the orbits 1 and 2 are chaotic, the orbits 3 and 4 are in order. Therefore, the system gradually shifts from chaotic to ordered regions with an increase of L . In Fig. 2(c), $E = 0.995$, $L = 4.6$, $a = 0.5$ and $\alpha = 0.2$. $\beta = 2 \times 10^{-4}$, $\beta = 5 \times 10^{-4}$, $\beta = 7 \times 10^{-4}$ and $\beta = 1 \times 10^{-3}$ correspond to four different orbits. When $\beta = 2 \times 10^{-4}$ or $\beta = 5 \times 10^{-4}$, the system is regular, while for $\beta = 7 \times 10^{-4}$ or $\beta = 1 \times 10^{-3}$, the system is chaotic. Thus, as β increases, the motion of the particle changes from order to chaos. In addition, the role of a is considered in Fig. 2(d). Here, $E = 0.995$, $L = 4.6$, $\beta = 3 \times 10^{-4}$, $\alpha = 0.2$ and $a \in [0.3, 0.9]$. When $a = 0.3$ and $a = 0.5$, the two orbits are chaotic, but when $a = 0.7$ and $a = 0.8$, they are orderly. Consequently, as a increases, the particle trajectories shift from chaos to order. Finally, the impact of parameter α is discussed in Fig. 2(e). Here, $E = 0.996$, $L = 4.6$, $\beta = 8.9 \times 10^{-4}$, $a = 0.5$ and $\alpha \in [0, 0.2]$. For $\alpha = 0.02$ or $\alpha = 0.06$, the orbit is regular, but for $\alpha = 0.13$ or $\alpha = 0.16$, the orbit is chaotic. It reveals that the motion of the particle transitions from order to chaos as α increases.

The conclusions from Poincaré sections can be validated by FLI. The dependence of FLI on various parameters after the integration time reaches $w = 10^7$ is shown in Fig. 3. Here, each circle represents a distinct orbit, and the values of parameters in Figs. 3(a)-3(e) are the same as in Figs. 2(a)-2(e). We estimate the FLIs of 30 trajectories in Fig. 3(a), the $FLIs \geq 8$ and $FLIs < 8$ correspond to the chaotic and regular orbits. The transition from order to chaos is observed clearly, $E = 0.9933$ and $E = 0.9966$ are the two thresholds. For $E \leq 0.993$, the system is in an ordered state, but for $E \geq 0.9969$, the system is in a chaotic state. However, when $0.9933 \leq E \leq 0.9966$, the dynamic evolution is very complex. For $0.9933 \leq E \leq 0.9945$, it is in a chaotic region; for $0.9948 \leq E \leq 0.9966$, it is in an ordered region. Overall, as the energy increases, the system transitions from order to chaos, but

there is an interval between the completely chaotic region and ordered region. The orbits in the interval are chaotic, but they are surrounded by the outside order region, they are still stable. This has been theoretically analyzed in [58]. Next, the FLIs of 20 trajectories are plotted in Fig. 3(b), the $FLIs \geq 20$ indicate the orbits are chaotic, while the $FLIs < 20$ indicate the orbits are regular. It can be seen that $L = 4.16$ is the threshold value, when L is below the threshold, the system is orderly; when L is above the threshold, the system is chaotic. In Fig. 3(c), where β is allowed to vary within the range $[1 \times 10^{-4}, 1 \times 10^{-3}]$. The FLIs of 30 different trajectories show that the transition from regular to chaotic regimes occurs at $\beta = 2.8 \times 10^{-4}$, $\beta = 4.3 \times 10^{-4}$, $\beta = 7 \times 10^{-4}$, and $\beta = 9.4 \times 10^{-4}$. In Fig. 3(d), chaos occurs in $a \leq 0.6$, whereas regular dynamics occur in $a > 0.6$. Thus, it is clear that the extent of chaos decreases as a increases. As illustrated in Fig. 3(e), when $\alpha < 0.1$, chaotic and ordered regions alternate; when $\alpha \geq 0.1$, the trajectories are chaotic. The reason for this has already been explained in previous [58].

(2) In case of $r=110$. In Fig. 4(a), the Poincaré sections of four orbits with $E = 0.991$, $E = 0.993$, $E = 0.997$ and $E = 0.998$ are analyzed, where the parameter settings are the same as those in Fig. 2(a). The orbits are regular for $E = 0.991$ and $E = 0.993$, while they are chaotic for $E = 0.997$ and $E = 0.998$. In contrast to Fig. 2(b), $E = 0.995$ and $a = 0.5$ are unchanged, while $\beta = 3 \times 10^{-4}$, $\alpha = 0.2$ and $L \in [4.0, 4.6]$ in Fig. 4(b). Here, when $L = 4.6$ and $L = 4.4$, the trajectories are in order. At $L = 4.3$, the trajectory is quasi-periodic, while at $L = 4.0$, the trajectory is evidently chaotic. Under the same parameter conditions, four different orbits are discussed in Fig. 4(c) to analyze the effect of β . The smooth curves (such as orbits 1 and 2) indicate that the motions of the orbits are regular at $\beta = 2 \times 10^{-4}$ and $\beta = 3 \times 10^{-4}$. On the other hand, there are many random discrete points in the phase diagram when the orbit takes value of $\beta = 7 \times 10^{-4}$ and $\beta = 8 \times 10^{-4}$. With respect to Fig. 2(d), a alters from 0.2 to 0.9 in Fig. 4(d). The orbits are in order at $a = 0.2$ and $a = 0.4$, while chaos emerges at $a = 0.7$ and $a = 0.8$. In Fig. 4(e), $E = 0.995$, $\beta = 5 \times 10^{-4}$, $L = 4.6$, $a = 0.5$, but α ranges from 0 to 0.2. When $\alpha = 0.02$ and $\alpha = 0.06$, the trajectories exhibit saddle-shaped patterns, indicating a regular behavior. However, at $\alpha = 0.14$ and $\alpha = 0.16$, the trajectories clearly display chaotic characteristics. In summary, the conclusions derived from Fig. 4 align with those of in Fig. 2.

In Fig. 5, the panels (a) and (c) depict the FLIs for 30 orbits, while the panels (b), (d), and (e) show the FLIs for 20 orbits. Here, the parameters are the same as those in

Fig. 4. The $FLIs \geq 30$ indicate chaos, while the $FLIs < 30$ indicate order in Fig. 5(a). The change from chaos to order takes place at $E = 0.9939$, when $E \geq 0.9939$, the system is mainly in a chaotic state, whereas when $E < 0.9939$, it is mostly in an ordered state. Therefore, as E increases, the system transitions from order to chaos, and the degree of chaos intensifies. In Figs. 5(b)-5(e), $FLI = 10$ is the boundary line between ordered and chaotic regions. When the $FLIs \geq 10$, the system indicates chaos, while the $FLIs < 10$ represent order. From Fig. 5(b), we can see that the transition from chaos to order occurs at $L = 4.36$ and $L = 4.48$. When $L < 4.36$, the system is in the chaotic region, whereas when $L \geq 4.48$, the system is in the ordered region. Thus, the system transitions from chaos to order as L increases. In Fig. 5(c), the system experiences a transition from order to chaos at $\beta = 3.4 \times 10^{-4}$. When $\beta < 3.4 \times 10^{-4}$, the system is mostly in ordered regions. Conversely, when $\beta \geq 3.4 \times 10^{-4}$, the system is predominantly in chaotic regions. Consequently, as the parameter β increases, the system transitions from ordered regions to chaotic regions, with the degree of chaos intensifying. In Fig. 5(d), the shift from chaotic to ordered regions happens at $a = 0.305$ and $a = 0.445$. When $a < 0.305$, the system is chaotic, and when $a \geq 0.445$, it is regular. Thus, as a increases, the system transitions from chaos to order. In Fig. 5(e), the shift from chaotic to regular dynamics occurs at $\alpha = 0.14$. For $\alpha < 0.14$, the system is primarily in an ordered area. However, the system is largely in chaotic regimes when $\alpha \geq 0.14$. Therefore, with an increase in α , the system transitions from order to chaos, and chaos becomes stronger.

In summary, when E , β , or α grows, the orbits have a transition from order to chaos; when L or a rises, the orbits have a transition from chaos to order.

B. The impact of two parameters acting simultaneously

In this section, the FLIs corresponding to two parameters are shown in Figs. 6-8. Here, the integration time is $w = 10^7$, the cyan and red represent the ordered and chaotic regions, respectively.

In Fig. 6(a), we set $L = 4.6$, $a = 0.5$ and $\alpha = 0.2$, a two-dimensional space (β, E) is given. Through aborative observation, we find that $FLI = 8$ is the threshold. In order to clearly see the boundaries between chaos and order in figures, we use 0 and 1 to denote regular and chaotic dynamics, respectively. It is easy to find that when E and β are small, the system

is in order. However, with the increase of E and β , the red area expands, which indicates a rise in chaos. There are two locally chaotic regions, one is $\beta \in [6.5 \times 10^{-4}, 8.5 \times 10^{-4}]$ and $E \in [0.9905, 0.9925]$, the other is $\beta \in [9.8 \times 10^{-4}, 1 \times 10^{-3}]$ and $E \in [0.990, 0.9905]$. In case of (β, L) , we set $E = 0.995$, $a = 0.5$ and $\alpha = 0.2$. The results are given in Fig. 6(b), here, the threshold is $FLI = 10$. Compared to Fig. 6(a), Fig. 6(b) does not have a complete chaotic region, the most areas are orderly, and there are only five local chaotic regions. As stated before [58], this situation is allowed. When $E = 0.995$, $L = 4.6$ and $\alpha = 0.2$, the parameter space (β, a) is considered in Fig. 6(c). Here, $FLI = 12$ is used as the threshold. Although most of the regions are orderly, there are still four chaotic regions. It can be seen that as β increases and a decreases, chaos gradually emerges and becomes more intense, which is the same as in Figs. 3(c)-3(d). Finally, the impact of the parameter space (β, α) on the dynamics is analyzed in Fig. 6(d). Here, $E = 0.995$, $L = 4.6$ and $a = 0.5$, the threshold is $FLI = 20$. There are five local chaotic regions, it reveals that the simultaneous increase of β and α has little effect on the chaotic behavior of the system.

The same as in Fig. 6, but the initial position of the particle is $r = 110$ in Fig. 7. $FLI = 30$ is selected as the boundary between order and chaos, and the two-dimensional parameter space (β, E) is shown in Fig. 7(a). It can be observed that the system mostly remains in ordered regions when both β and E are small. As β and E gradually increase, the system has a transition from ordered to chaotic regions. Chaos starts to appear when $E = 0.9915$. When $E < 0.9915$, the system is orderly regardless of how β changes. When $E \geq 0.9915$, the red area gradually expands as E and β increase, which indicates an increase in chaos. Besides, there are two local ordered regions. The first is $\beta \in [6.5 \times 10^{-4}, 7.5 \times 10^{-4}]$ and $E \in [0.9975, 0.9985]$, while the second is $\beta \in [9.5 \times 10^{-4}, 1 \times 10^{-3}]$ and $E \in [0.9945, 0.9955]$. In Figs. 7(b)-7(d), $FLI = 10$ is the threshold. The two-dimensional parameter space (β, L) is presented in Fig. 7(b). The system is regular when $L < 3.95$, while chaos begins to appear when $L \geq 3.95$. Unlike in Fig. 7(a), there are only two local chaotic regions, corresponding to $\beta \in [2.5 \times 10^{-4}, 3.5 \times 10^{-4}]$, $L \in [3.95, 4.35]$ and $\beta \in [3.5 \times 10^{-4}, 1 \times 10^{-3}]$, $L \in [4.25, 4.6]$. As β increases, the red region expands, indicating a rise in chaos. However, chaos also appears when L increases, which is contrary to the conclusions from Fig. 5(b). The reason for this is that when β and L are considered simultaneously, the system is primarily influenced by β . The two-dimensional parameter space (β, a) in Fig. 7(c) reveals that the system is almost in order, such as $a < 0.15$, $0.25 < a < 0.35$ or $\beta < 2.5 \times 10^{-4}$. The shift from order to chaos

only occurs at $a = 0.15$ and $a = 0.35$. When $a < 0.35$, there is a local chaotic region when $\beta \in [2.5 \times 10^{-4}, 3.5 \times 10^{-4}]$ and $a \in [0.15, 0.25]$. For $a \geq 0.35$, it is apparent that increasing β intensifies the chaos. In contrast, as a increases, the ordered region expands and chaos weakens. As shown in Fig. 7(d), the system is ordered when $\beta < 3.5 \times 10^{-4}$, with chaos beginning at $\beta = 3.5 \times 10^{-4}$. Moreover, for $\beta \geq 3.5 \times 10^{-4}$, increasing α expands the red regions, which corresponds to a stronger chaotic behavior.

In the left panels of Fig. 8, the initial values are $r = 11$ and $\theta = \pi/2$, whereas in the right panels in Fig. 8, the initial values are $r = 110$ and $\theta = \pi/2$. The parameter space (α, E) is discussed in Figs. 8(a)-8(b). Here, $L = 4.6$, $\beta = 8.9 \times 10^{-4}$, $a = 0.5$. In Fig. 8(a), $FLI = 10$ is adopted as the threshold; while in Fig. 8(b), the threshold is $FLI = 20$. In Fig. 8(a), the system generates chaos at $E = 0.9955$. When $E < 0.9955$, the system is mostly in order, except in two intervals where local chaos exists. That is, for $E \in [0.9905, 0.9915]$, there are two regions where local chaos exists approximately within $\alpha \in [0.11, 0.13]$ and $\alpha \in [0.17, 0.19]$. When $E \geq 0.9955$, chaos intensifies as α increases. However, the difference from Fig. 8(a) is that chaos appears in Fig. 8(b) when $E = 0.9915$. When $E < 0.9915$, no matter how β varies, the system is in order all the time. The results show that chaos gets enhanced with the simultaneous increase of both E and α . Figs. 8(c)-8(d) focus on the parameter space (α, L) , with the rest parameters are $E = 0.995$, $\beta = 8.9 \times 10^{-4}$ and $a = 0.5$. Here, $FLI = 20$ and $FLI = 50$ are used as the thresholds. In Fig. 8(c), the system is mainly in order, but there are two local chaotic regions, one is $\alpha \in [0.03, 0.09]$ and $L \in [3.55, 4.15]$, the other is $\alpha \in [0.11, 0.15]$ and $L \in [3.85, 4.05]$. However, a large area of chaotic regions can be observed in Fig. 8(d). When $\alpha < 0.03$ or $L \geq 4.45$, regardless of how the other parameter changes, the system is in a chaotic state. As for the case where $\alpha \in [0.03, 0.2]$ and $L \in [3.5, 4.45]$, with the simultaneous increase of L and α , the ordered region expands and chaos diminishes. These indicate that when L and α change simultaneously, the system is mainly influenced by the parameter L . Finally, we analyze the parameter space (α, a) in Figs. 8(e)-8(f), where $E = 0.995$, $L = 4.6$ and $\beta = 8.9 \times 10^{-4}$. $FLI = 20$ and $FLI = 50$ are served as the thresholds. There are merely two tiny chaotic regions in Fig. 8(e). The first occurs where $\alpha \in [0.17, 0.19]$ and $a \in [0.25, 0.35]$, while the second exists when $\alpha \in [0.19, 0.2]$ and $a \in [0.35, 0.45]$. In Fig. 8(f), the system is chaotic when $\alpha < 0.11$ or $a > 0.35$. For $\alpha \in [0.11, 0.2]$ and $a \in [0, 0.35]$, as both a and α increase simultaneously, the ordered region expands and chaos weakens. The results clearly demonstrate that the role of a is more

significant than α .

From the chaotic dynamics of the charged particle, we find that different parameters have different impacts on the motion of the particle. When one of the parameters is taken into account, for E , β , or α increases, the system shifts from order to chaos. But for L or a increases, the opposite occurs. However, When any two of them are considered simultaneously, the situation is quite complicated. For example, if β and L cooperate with each other, β has a greater impact on the system than L . When L and α function at the same time, L predominates. Similarly, when a and α interact with each other, a is more important. At last, we find that the motion of the particle has a relatively small dependence on the modified gravitational parameter α .

V. CONCLUSIONS

The chaotic motion of the charged test particle in Kerr-MOG black hole is discussed in this paper. Due to the non-integrable of Kerr-MOG black hole in the presence of an external magnetic field, we adopt a time transformation function to convert the original Hamiltonian. The new Hamiltonian can be decomposed into five integrable parts to construct explicit symplectic algorithms. After that, three kinds of explicit symplectic methods are proposed. Numerical experiments show that PRK_64 is the best method and has significant advantages such as the stability and accuracy in long-term numerical integration. Thus, PRK_64 is used to explore the chaotic motion of a charged particle around Kerr-MOG black hole. With the help of the Poincaré sections and the fast Lyapunov indicators, effects of E , L , a , α and β on chaos are discussed in detail. The results show that the chaotic area increases as E , β or α increases, but a and L are not like that. When multiple parameters are applied simultaneously, we find that a and L play a major role. These findings are useful for understanding dynamics of the charged particles in modified gravity theories, and they provide a new perspective to analyze the chaotic motion in strong gravitational field. It should be emphasized that the accuracy and stability of numerical algorithms are crucial for discussing the chaotic motion of particles in strong gravitational fields. This is because only algorithms with high accuracy and good stability can avoid the pseudo chaos [55]. Therefore, the time transformation method and Hamiltonian decomposition method are useful.

ACKNOWLEDGMENTS

This work is supported by the Natural Science Foundation of China under Grant Nos. 12073008, 12473074, 11703005.

Data Availability Statement: This manuscript has no associated data or the data will not be deposited. [Author’s comment: All of the data are shown as the figures and formula. No other associated data.]

Code Availability Statement: Code/software will be made available on reasonable request. [Author’s comment: The code/software generated during and/or analysed during the current study is available from the first author Zhenmeng Xu on reasonable request.]

-
- [1] R. Caldwell and M. Kamionkowski, “Dark matter and dark energy,” *Nature* **458**, 587–589 (2009), doi:10.1038/458587a.
 - [2] F. Camilloni, T. Harkmark, M. Orselli, and M. J. Rodriguez, “Blandford-Znajek jets in Modified Gravity,” *JCAP* **01** (2024), 047, doi:10.1088/1475-7516/2024/01/047, [arXiv:2307.06878 [gr-qc]].
 - [3] P. Jai-akson, A. Chatrabhuti, O. Evnin, and L. Lehner, “Black hole merger estimates in Einstein-Maxwell and Einstein-Maxwell-dilaton gravity,” *Phys. Rev. D* **96**, no.4, 044031 (2017), doi:10.1103/PhysRevD.96.044031 [arXiv:1706.06519 [gr-qc]].
 - [4] P. J. E. Peebles and B. Ratra, “The Cosmological Constant and Dark Energy,” *Rev. Mod. Phys.* **75**, 559–606 (2003), doi:10.1103/RevModPhys.75.559 [arXiv:astro-ph/0207347 [astro-ph]].
 - [5] M. Milgrom, “A Modification of the Newtonian dynamics as a possible alternative to the hidden mass hypothesis,” *Astrophys. J.* **270**, 365–370 (1983), doi:10.1086/161130.
 - [6] J. W. Moffat, “Scalar-tensor-vector gravity theory,” *JCAP* **03**, 004 (2006), doi:10.1088/1475-7516/2006/03/004 [arXiv:gr-qc/0506021 [gr-qc]].
 - [7] J. W. Moffat and S. Rahvar, “The MOG weak field approximation and observational test of galaxy rotation curves,” *Mon. Not. Roy. Astron. Soc.* **436**, 1439–1451 (2013), doi:10.1093/mnras/stt1670 [arXiv:1306.6383 [astro-ph.GA]].
 - [8] J. W. Moffat and S. Rahvar, “The MOG weak field approximation – II. Observational

- test of Chandra X-ray clusters,” *Mon. Not. Roy. Astron. Soc.* **441**, 3724–3732 (2014), doi:10.1093/mnras/stu855 [arXiv:1309.5077 [astro-ph.CO]].
- [9] J. R. Brownstein and J. W. Moffat, “Galaxy cluster masses without non-baryonic dark matter,” *Mon. Not. Roy. Astron. Soc.* **367**, 527–540 (2006), doi:10.1111/j.1365-2966.2006.09996.x [arXiv:astro-ph/0507222 [astro-ph]].
- [10] J. W. Moffat and V. T. Toth, “Rotational velocity curves in the Milky Way as a test of modified gravity,” *Phys. Rev. D* **91**, 043004 (2015), doi:10.1103/PhysRevD.91.043004 [arXiv:1411.6701 [astro-ph.GA]].
- [11] J. W. Moffat, “Structure growth and the CMB in modified gravity (MOG),” [arXiv:1409.0853 [astro-ph.CO]].
- [12] J. W. Moffat, “Scalar and vector field constraints, deflection of light and lensing in modified gravity (MOG),” [arXiv:1410.2464 [gr-qc]].
- [13] J. W. Moffat, “Modified gravity black holes and their observable shadows,” *Eur. Phys. J. C* **75**, 130 (2015), doi:10.1140/epjc/s10052-015-3352-6 [arXiv:1502.01677 [gr-qc]].
- [14] H. C. Lee and Y. J. Han, “Innermost stable circular orbit of Kerr-MOG black hole,” *Eur. Phys. J. C* **77** (2017) no.10, 655, doi:10.1140/epjc/s10052-017-5152-7 [arXiv:1704.02740 [gr-qc]].
- [15] M. Y. Guo, N. A. Obers, and H. P. Yan, “Observational signatures of near-extremal Kerr-like black holes in a modified gravity theory at the Event Horizon Telescope,” *Phys. Rev. D* **98**, no. 8, 084063 (2018), doi:10.1103/PhysRevD.98.084063, [arXiv:1806.05249 [gr-qc]].
- [16] Y. H. Hou, Z. Y. Zhang, H. P. Yan, M. Y. Guo, and B. Chen, “Image of a Kerr-Melvin black hole with a thin accretion disk,” *Phys. Rev. D* **106**, no. 6, 064058 (2022), doi:10.1103/PhysRevD.106.064058, [arXiv:2206.13744 [gr-qc]].
- [17] E. Battista and G. Esposito, “Geodesic motion in Euclidean Schwarzschild geometry,” *Eur. Phys. J. C* **82**, no. 12, 1088 (2022), doi:10.1140/epjc/s10052-022-11070-w, [arXiv:2202.03763 [gr-qc]].
- [18] P. Dutta, K. L. Panigrahi, and B. Singh, “Chaos Bound and its violation in Black p-brane,” [arXiv:2408.14056 [hep-th]].
- [19] S. Dalui, B. R. Majhi, and P. Mishra, “Presence of horizon makes particle motion chaotic,” *Phys. Lett. B* **788** (2019), 486–493, doi:10.1016/j.physletb.2018.11.050, [arXiv:1803.06527 [gr-qc]].
- [20] S. Dalui, B. R. Majhi, and P. Mishra, “Induction of chaotic fluctuations in particle dynam-

- ics in a uniformly accelerated frame,” *Int. J. Mod. Phys. A* **35**, no. 18, 2050081 (2020), doi:10.1142/S0217751X20500815, [arXiv:1904.11760 [gr-qc]].
- [21] D. Z. Ma, X. Wu, and J. F. Zhu, “Velocity scaling method to correct individual Kepler energies,” *New Astron.* **13**, no. 4, 216–223 (2008), doi:10.1016/j.newast.2007.09.002.
- [22] J. M. Sanz-Serna, “Symplectic integrators for Hamiltonian problems: an overview,” *Acta Numer.* **1**, 243–286 (1992), doi:10.1017/S0962492900002282.
- [23] K. Feng, “On difference schemes and symplectic geometry,” in *Proceedings of the 5th International Symposium on Differential Geometry and Differential Equations* (1984).
- [24] R. D. Ruth, “A Canonical Integration Technique,” *IEEE Trans. Nucl. Sci.* **30**, no. 4, 2669–2671 (1983), doi:10.1109/TNS.1983.4332919.
- [25] X. H. Liao, “Symplectic integrator for general near-integrable Hamiltonian system,” *Celestial Mech. Dyn. Astron.* **66**, no. 3, 243–253 (1996), doi:10.1007/BF00049381.
- [26] M. Suzuki, “Fractal decomposition of exponential operators with applications to many-body theories and Monte Carlo simulations,” *Phys. Lett. A* **146**, no. 6, 319–323 (1990), doi:10.1016/0375-9601(90)90962-N.
- [27] X. Wu and Y. Xie, “Symplectic structure of post-Newtonian Hamiltonian for spinning compact binaries,” *Phys. Rev. D* **81**, no. 8, 084045 (2010), doi:10.1103/PhysRevD.81.084045.
- [28] S. Y. Zhong and X. Wu, “Manifold corrections on spinning compact binaries,” *Phys. Rev. D* **81**, no. 10, 104037 (2010), doi:10.1103/PhysRevD.81.104037.
- [29] S. Y. Zhong, X. Wu, S. Q. Liu, and X. F. Deng, “Global symplectic structure-preserving integrators for spinning compact binaries,” *Phys. Rev. D* **82**, no. 12, 124040 (2010), doi:10.1103/PhysRevD.82.124040.
- [30] X. Wu and S. Y. Zhong, “Regular dynamics of canonical post-Newtonian Hamiltonian for spinning compact binaries with next-to-leading order spin-orbit interactions,” *Gen. Rel. Grav.* **43**, no. 8, 2185–2198 (2011), doi:10.1007/s10714-011-1171-0.
- [31] L. J. Mei, M. J. Ju, X. Wu, and S. Q. Liu, “Dynamics of spin effects of compact binaries,” *Mon. Not. R. Astron. Soc.* **435**, no. 3, 2246–2255 (2013), doi:10.1093/mnras/stt1441.
- [32] L. J. Mei, X. Wu, and F. Y. Liu, “On preference of Yoshida construction over Forest–Ruth fourth-order symplectic algorithm,” *Eur. Phys. J. C* **73**, no. 5, 2413 (2013), doi:10.1140/epjc/s10052-013-2413-y.
- [33] M. Preto and P. Saha, “On post-Newtonian orbits and the Galactic-center stars,” *Astrophys. J.*

- 703**, 1743–1751 (2009), doi:10.1088/0004-637X/703/2/1743 [arXiv:0906.2226 [astro-ph.GA]].
- [34] J. Wisdom and M. Holman, “Symplectic maps for the n-body problem,” *Astron. J.* **102**, 1528–1538 (1991), doi:10.1086/115978.
- [35] S. A. Chin, “Symplectic integrators from composite operator factorizations,” *Phys. Lett. A* **226**, no. 6, 344–348 (1997), doi:10.1016/S0375-9601(97)00003-0.
- [36] S. A. Chin and C. R. Chen, “Forward Symplectic Integrators for Solving Gravitational Few-Body Problems,” *Celest. Mech. Dyn. Astron.* **91**, no. 3-4, 301–322 (2005), doi:10.1007/s10569-004-4622-z [arXiv:astro-ph/0304223 [astro-ph]].
- [37] W. Sun, X. Wu, and G. Q. Huang, “Symplectic integrators with potential derivatives to third order,” *Res. Astron. Astrophys.* **11**, no. 3, 353–368 (2021), doi:10.1088/1674-4527/11/3/009.
- [38] X. Wu, Y. Wang, W. Sun, F. Y. Liu, and D. Z. Ma, “Explicit Symplectic Integrators with Adaptive Time Steps in Curved Spacetimes,” *Astrophys. J. Suppl.* **275**, no. 2, 31 (2024), doi:10.3847/1538-4365/ad8351 [arXiv:2412.01045 [gr-qc]].
- [39] Y. Wang, W. Sun, F. Y. Liu, and X. Wu, “Construction of Explicit Symplectic Integrators in General Relativity. I. Schwarzschild Black Holes,” *Astrophys. J.* **907**, no. 2, 66 (2021), doi:10.3847/1538-4357/abcb8d [arXiv:2102.00373 [gr-qc]].
- [40] Y. Wang, W. Sun, F. Y. Liu, and X. Wu, “Construction of Explicit Symplectic Integrators in General Relativity. II. Reissner–Nordström Black Holes,” *Astrophys. J.* **909**, no. 1, 22 (2021), doi:10.3847/1538-4357/abd701 [arXiv:2103.02864 [gr-qc]].
- [41] Y. Wang, W. Sun, F. Y. Liu, and X. Wu, “Construction of Explicit Symplectic Integrators in General Relativity. III. Reissner–Nordström–(anti)-de Sitter Black Holes,” *Astrophys. J. Suppl.* **254**, no. 1, 8 (2021), doi:10.3847/1538-4365/abf116 [arXiv:2103.12272 [gr-qc]].
- [42] X. Wu, Y. Wang, W. Sun, and F. Y. Liu, “Construction of Explicit Symplectic Integrators in General Relativity. IV. Kerr Black Holes,” *Astrophys. J.* **914**, no. 1, 63 (2021), doi:10.3847/1538-4357/abfc45 [arXiv:2106.12356 [gr-qc]].
- [43] S. Mikkola, “Practical Symplectic Methods with Time Transformation for the Few-Body Problem,” *Celest. Mech. Dyn. Astron.* **67**, no. 2, 145–165 (1997), doi:10.1023/A:1008217427749.
- [44] A. R. Hu and G. Q. Huang, “Chaos in a Magnetized Brane-World Spacetime Using Explicit Symplectic Integrators,” *Universe* **8**, no. 7, 369 (2022), doi:10.3390/universe8070369.
- [45] N. Y. Zhou, H. X. Zhang, X. Sun, W. F. Liu, and D. Li, “Chaotic Motion of Charged Test Particles in a Magnetized Schwarzschild Black Hole,” *Acta Astron. Sin.* **64**, no. 4, 39 (2023),

doi:10.15940/j.cnki.0001-5245.2023.04.002.

- [46] W. F. Cao, X. Wu, and J. Lyu, “Electromagnetic field and chaotic charged-particle motion around hairy black holes in Horndeski gravity,” *Eur. Phys. J. C* **84**, no. 4, 435 (2024), doi:10.1140/epjc/s10052-024-12804-8 [arXiv:2404.19225 [gr-qc]].
- [47] J. J. Lu and X. Wu, “Effects of Two Quantum Correction Parameters on Chaotic Dynamics of Particles near Renormalized Group Improved Schwarzschild Black Holes,” *Universe* **10**, no. 7, 277 (2024), doi:10.3390/universe10070277 [arXiv:2406.18943 [gr-qc]].
- [48] D. Z. Ma, J. P. Wu, and J. F. Zhang, “Chaos from the ring string in a Gauss-Bonnet black hole in AdS5 space,” *Phys. Rev. D* **89**, no. 8, 086011 (2014), doi:10.1103/PhysRevD.89.086011 [arXiv:1405.3563 [hep-th]].
- [49] J. R. Mureika, J. W. Moffat, and M. Faizal, “Black hole thermodynamics in Modified Gravity (MOG),” *Phys. Lett. B* **757**, 528-536 (2016), doi:10.1016/j.physletb.2016.04.041 [arXiv:1504.08226 [gr-qc]].
- [50] Z. L. Zhang, S. B. Chen, and J. L. Jing, “Images of Kerr-MOG black holes surrounded by geometrically thick magnetized equilibrium tori,” *JCAP* **09**, 027 (2024), doi:10.1088/1475-7516/2024/09/027 [arXiv:2404.12223 [gr-qc]].
- [51] S. U. Khan, J. Rayimbaev, and Z. Stuchlík, “Charged particle motion and acceleration around Kerr-MOG black hole,” [arXiv:2311.16936 [gr-qc]].
- [52] R. M. Wald, “Black hole in a uniform magnetic field,” *Phys. Rev. D* **10**, no. 6, 1680–1685 (1974), doi:10.1103/PhysRevD.10.1680.
- [53] H. Yoshida, “Construction of higher order symplectic integrators,” *Phys. Lett. A* **150**, no. 5, 262–268 (1990), doi:10.1016/0375-9601(90)90092-3.
- [54] N. Y. Zhou, H. X. Zhang, W. F. Liu, and X. Wu, “A Note on the Construction of Explicit Symplectic Integrators for Schwarzschild Spacetimes,” *Astrophys. J.* **927**, no. 2, 160 (2022), doi:10.3847/1538-4357/ac497f.
- [55] D. Z. Ma, D. Zhang, G. Y. Fu, and J. P. Wu, “Chaotic dynamics of string around charged black brane with hyperscaling violation,” *JHEP* **01**, 103 (2020), doi:10.1007/JHEP01(2020)103 [arXiv:1911.09913 [hep-th]].
- [56] C. Froeschlé and E. Lega, “On the Structure of Symplectic Mappings. The Fast Lyapunov Indicator: a Very Sensitive Tool,” *Celest. Mech. Dyn. Astron.* **78**, 167–195 (2000), doi:10.1023/A:1011141018230.

- [57] X. Wu, T. Y. Huang, and H. Zhang, “Lyapunov indices with two nearby trajectories in a curved spacetime,” *Phys. Rev. D* **74**, 083001 (2006), doi:10.1103/PhysRevD.74.083001 [arXiv:1006.5251 [gr-qc]].
- [58] A. Giorgilli, U. Locatelli, and M. Sansottera, “Secular dynamics of a planar model of the Sun-Jupiter-Saturn-Uranus system; effective stability in the light of Kolmogorov and Nekhoroshev theories,” *Regul. Chaotic Dyn.* **22**, no. 1, 54–77 (2017), doi:10.1134/S156035471701004X [arXiv:1702.04894 [math-ph]].

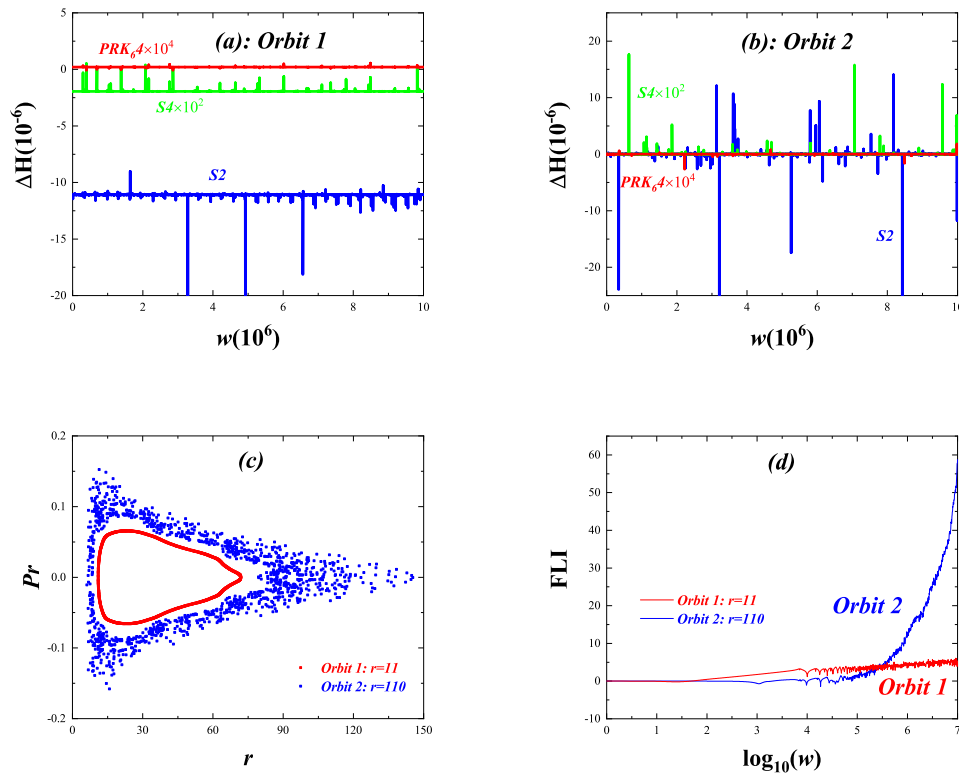


FIG. 1. (a) and (b) are the Hamiltonian error $\Delta\mathcal{H}$ for $S2$, $S4$, and PRK_64 . Here, the step size is $h = 1$, the other parameters are $E = 0.995$, $L = 4.6$, $\beta = 4 \times 10^{-4}$, $a = 0.5$, and $\alpha = 0.2$. (a) is related to the orbit 1, and (b) deals with the orbit 2. (c) Poincaré sections of the two orbits at $\theta = \pi/2$ and $p_\theta > 0$. (d) FLIs of the two orbits.

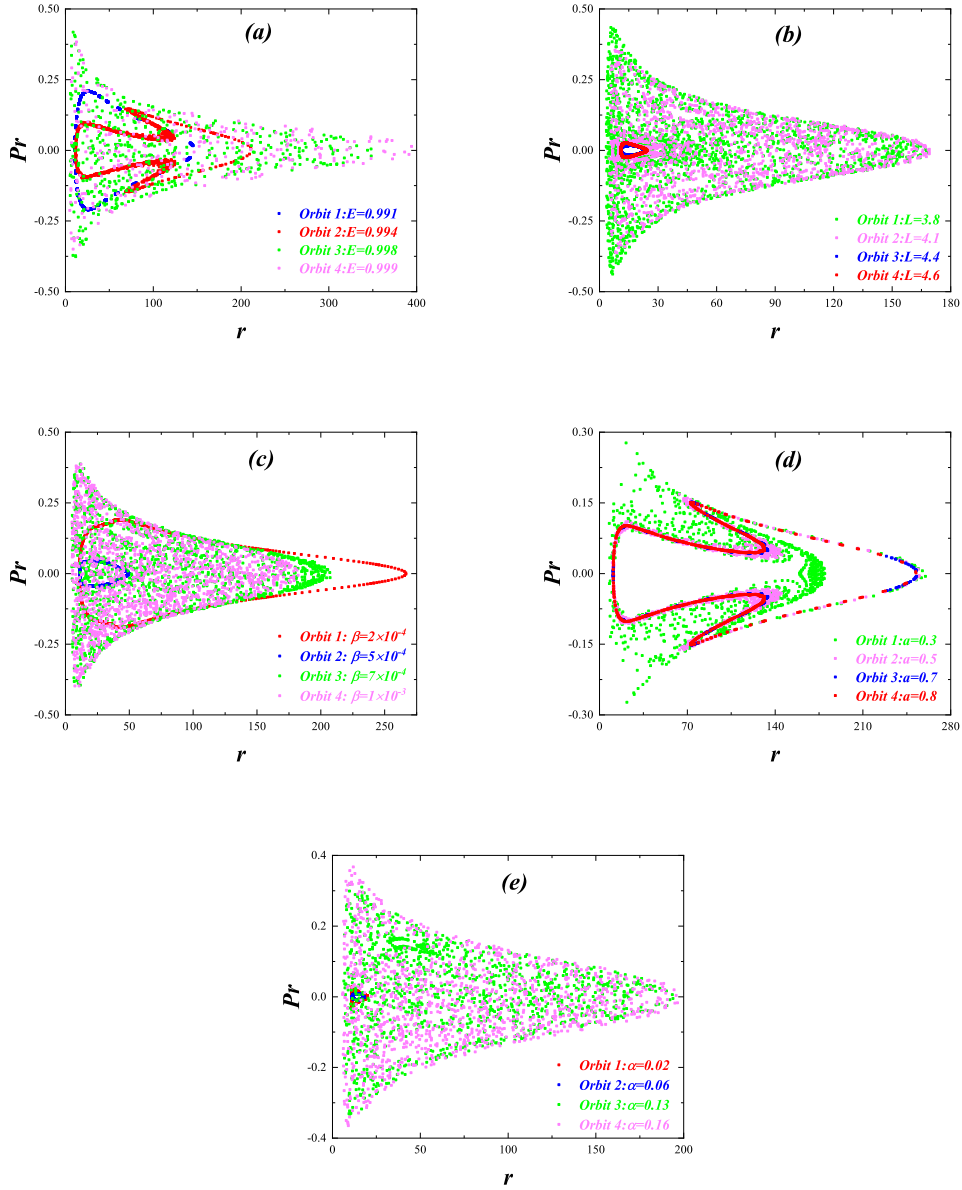


FIG. 2. Poincaré sections for different orbits at $r = 11$ with varying parameters. Here, each figure contains four different motion trajectories. (a) $L = 4.6$, $\beta = 4 \times 10^{-4}$, $a = 0.5$ and $\alpha = 0.2$. (b) $E = 0.995$, $a = 0.5$, $\alpha = 0.08$ $\beta = 8.9 \times 10^{-4}$. (c) $E = 0.995$, $L = 4.6$, $a = 0.5$ and $\alpha = 0.2$. (d) $E = 0.995$, $L = 4.6$, $\beta = 3 \times 10^{-4}$ and $\alpha = 0.2$. (e) $E = 0.996$, $L = 4.6$, $\beta = 8.9 \times 10^{-4}$ and $a = 0.5$.

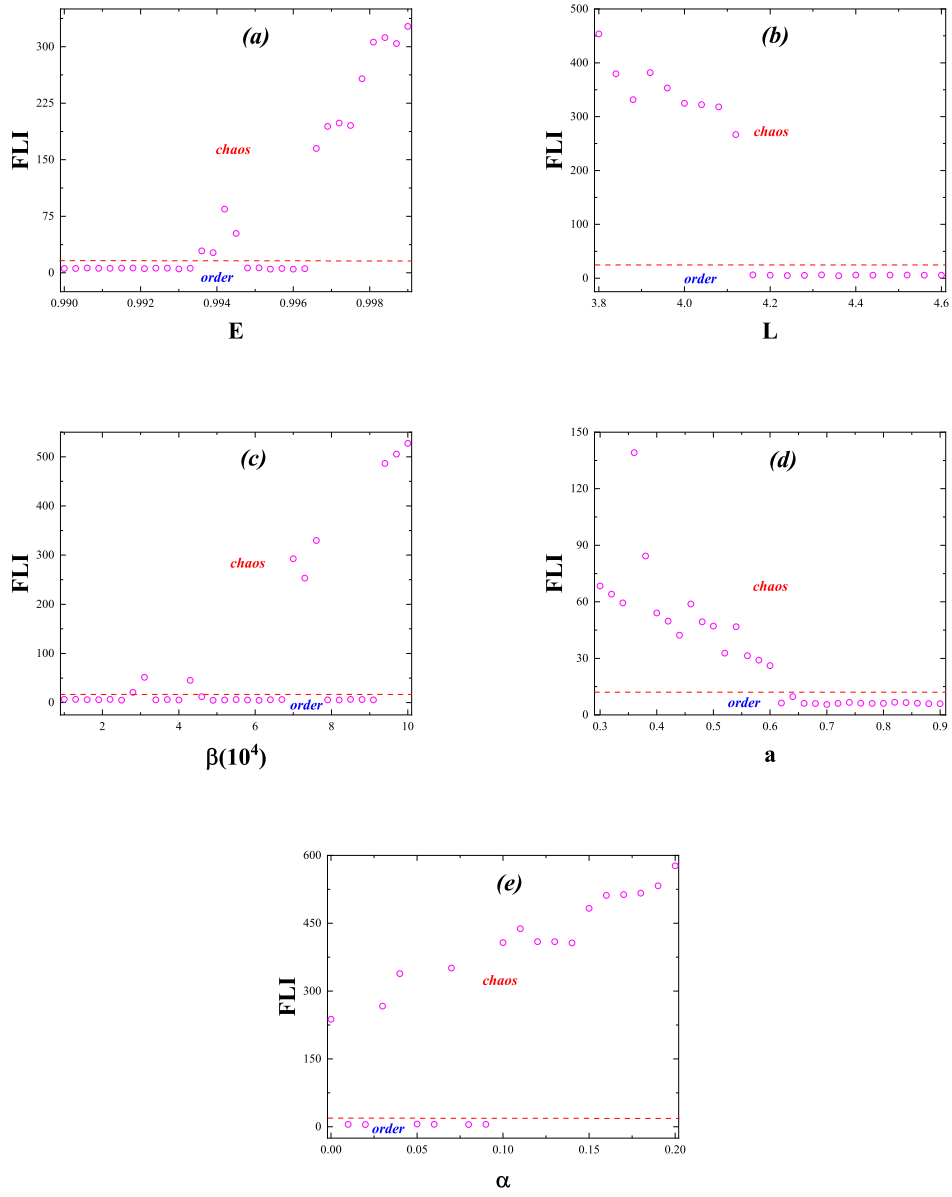


FIG. 3. The same as Figure 2, but for FLI. Here, $r = 11$, the integration time is $w = 10^7$.

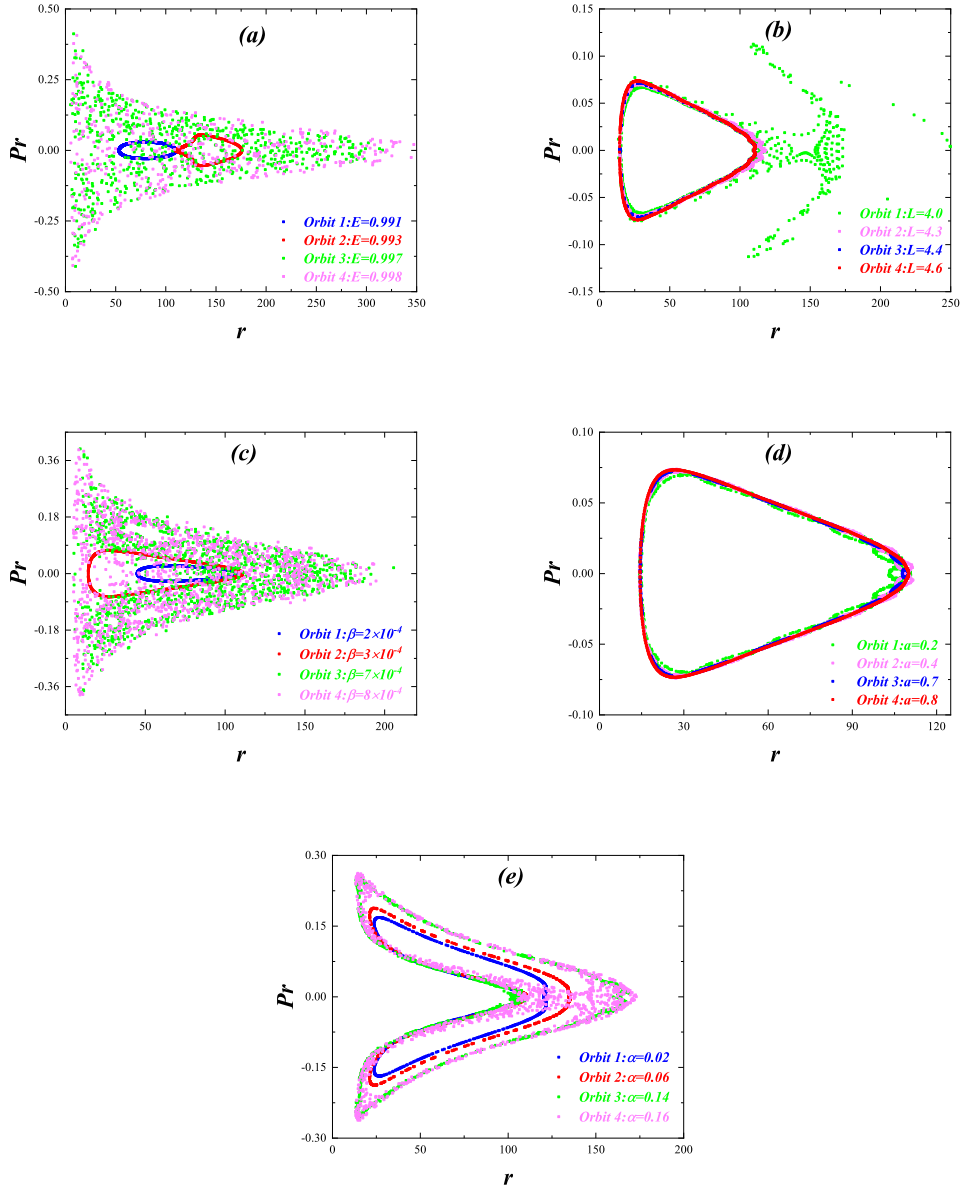


FIG. 4. Poincaré sections of the orbits at $r = 110$ with different parameters. Here, each figure contains four different motion trajectories. (a) $L = 4.6$, $\beta = 4 \times 10^{-4}$, $a = 0.5$ and $\alpha = 0.2$. (b) $E = 0.995$, $a = 0.5$, $\alpha = 0.2$ and $\beta = 3 \times 10^{-4}$, (c) $E = 0.995$, $L = 4.6$, $a = 0.5$ and $\alpha = 0.2$. (d) $E = 0.995$, $L = 4.6$, $\beta = 3 \times 10^{-4}$ and $\alpha = 0.2$. (e) $E = 0.995$, $L = 4.6$, $\beta = 5 \times 10^{-4}$ and $a = 0.5$.

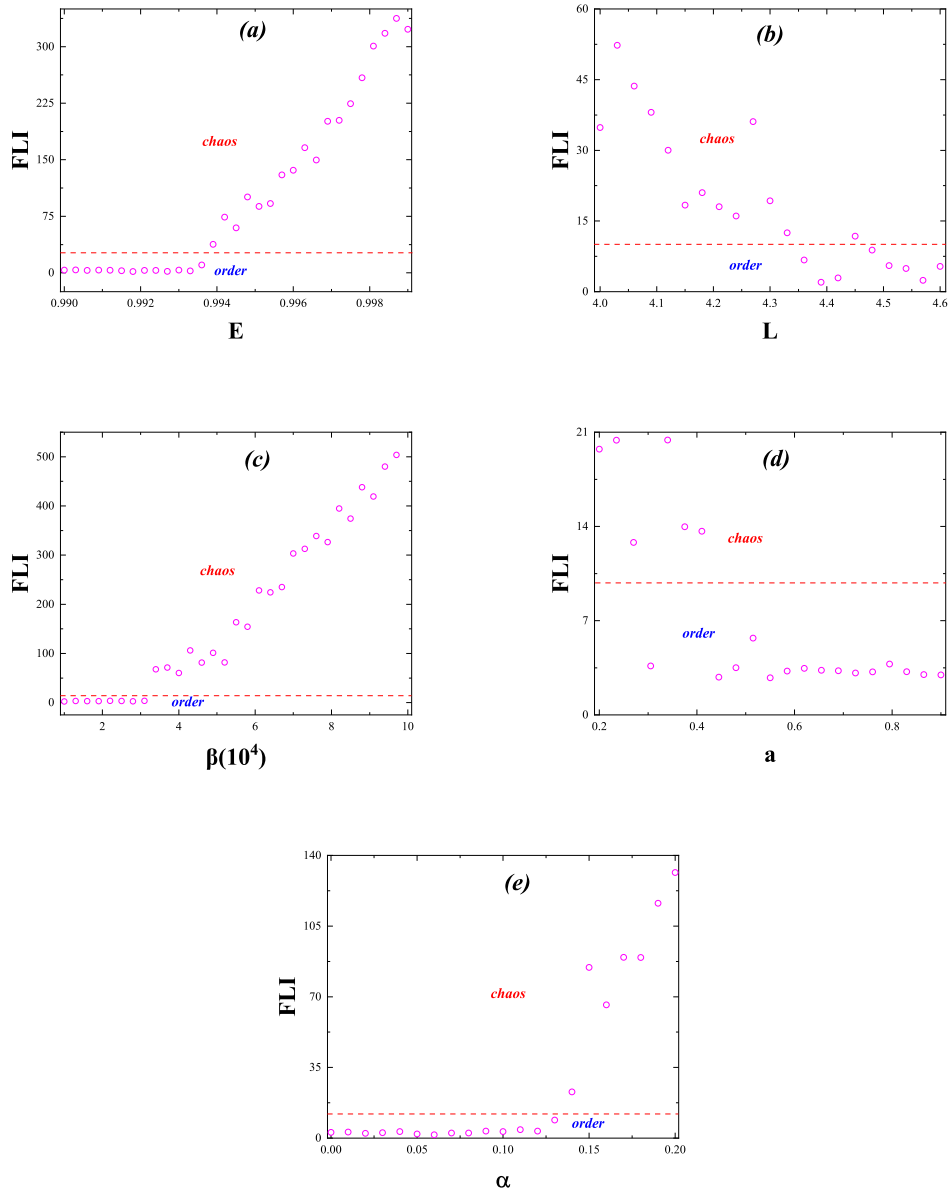


FIG. 5. The same as Figure 4, but for FLI.

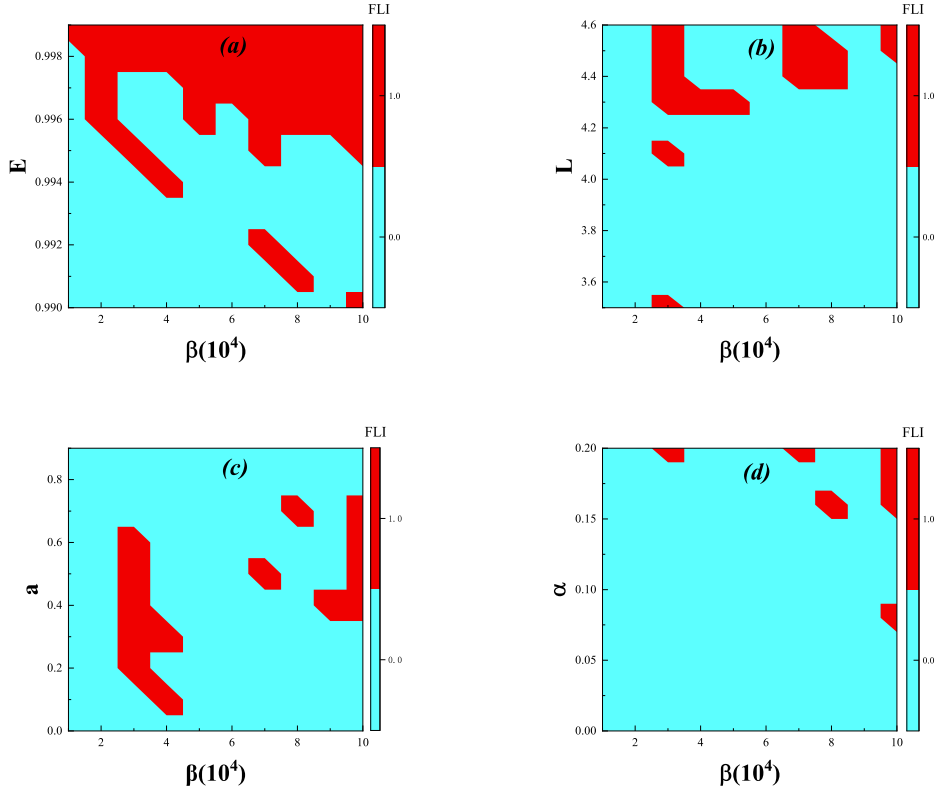


FIG. 6. The FLI distribution in two-dimensional parameter spaces when $r = 11$. Here, the integration time is $w = 10^7$, 0 and 1 denote regular and chaos, respectively. The colors in cyan and red represent the regular and chaotic regions, respectively. **(a)** The parameter space is (β, E) , in which $L = 4.6$, $a = 0.5$ and $\alpha = 0.2$. **(b)** The parameter space is (β, L) , the other parameters are $E = 0.995$, $a = 0.5$ and $\alpha = 0.2$. **(c)** The parameter space is (β, a) , with other parameters are fixed at $E = 0.995$, $L = 4.6$ and $\alpha = 0.2$. **(d)** The parameter space is (β, α) , and the rest parameters are $E = 0.995$, $L = 4.6$ and $a = 0.5$.

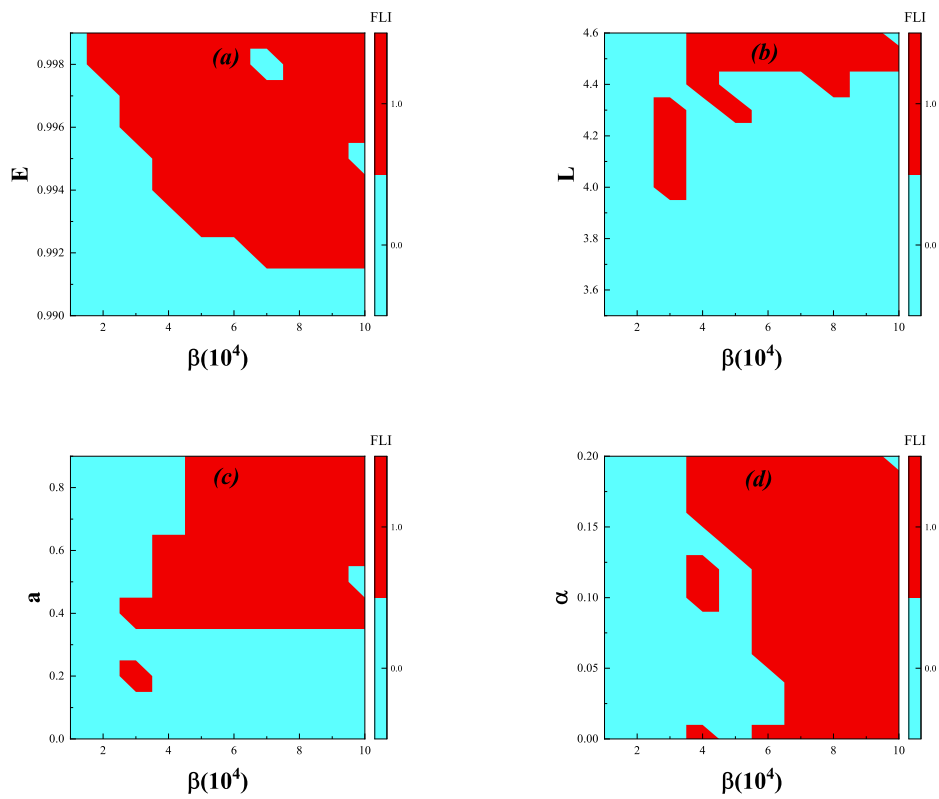


FIG. 7. The same as Figure 6, but for $r = 110$.

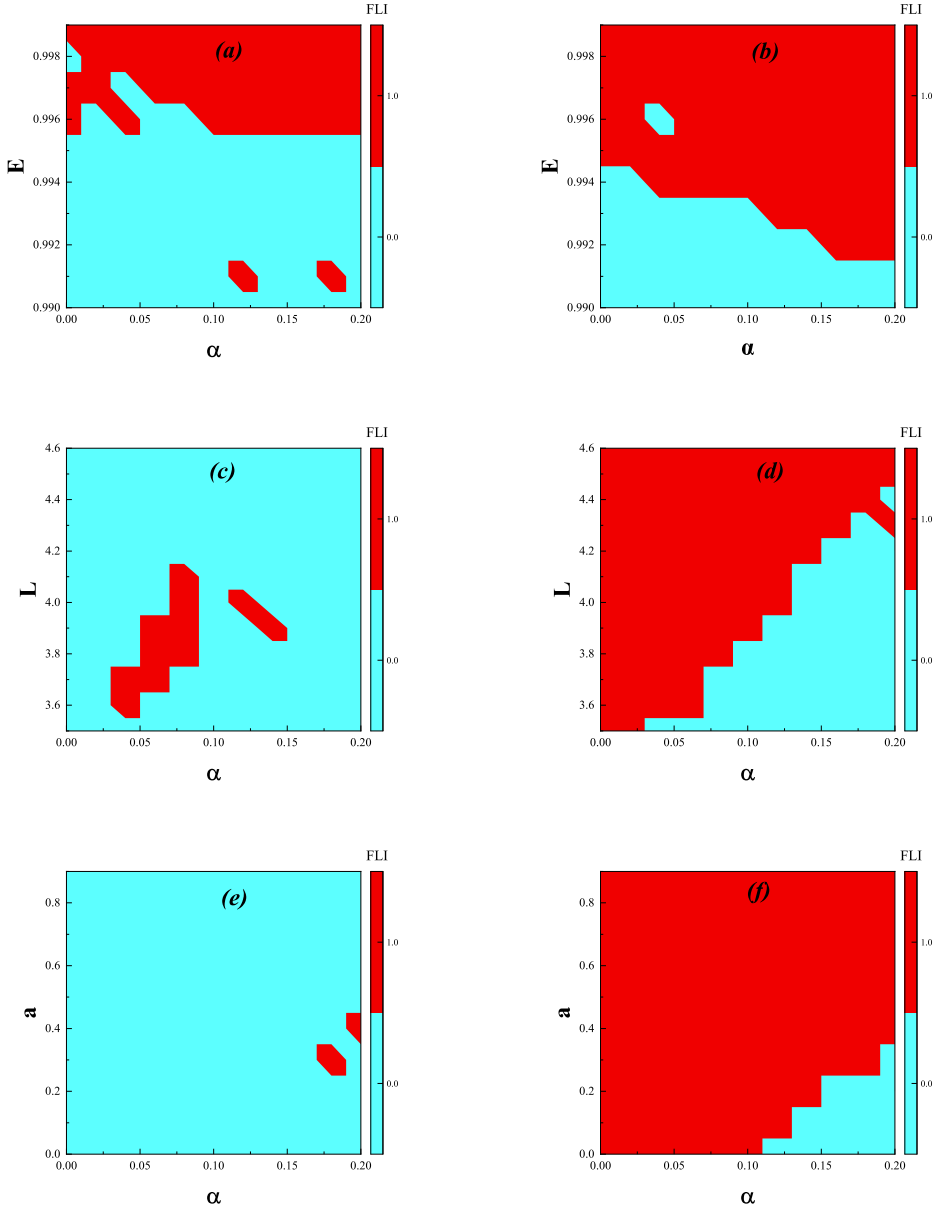


FIG. 8. The FLI distribution in two-dimensional parameter spaces. In panels a, c and e, the initial values are $r = 11$ and $\theta = \pi/2$, whereas in panels b, d and f, we take $r = 110$ and $\theta = \pi/2$ as the initial values. In (a) and (b), the parameter space is (α, E) , and $L = 4.6$, $\beta = 8.9 \times 10^{-4}$ and $a = 0.5$. In (c) and (d), the parameter space is (α, L) , with $E = 0.995$, $\beta = 8.9 \times 10^{-4}$ and $a = 0.5$. In (e) and (f), the parameter space is (α, a) , and the other parameters are $E = 0.995$, $L = 4.6$ and $\beta = 8.9 \times 10^{-4}$.